Estimation of mineral accessible surface area from mineral abundance and clay content

*Fanqi Qin‡, Md. Fahim Salek‡, Parisa Asadi, Chidera Iloejesi, Olivia Brunhoeber, Mukseet Mahmood, Lauren, E. Beckingham**

Department of Civil and Environmental Engineering, Auburn University

Auburn, AL 36830

*Corresponding author: leb@auburn.edu

‡co-first author, these authors contributed equally towards this work

Abstract

Mineral reactive surface area is often quantified through a wide range of approaches (e.g., BET adsorption, geometry approximation, imaging techniques). As such, values vary 1 – 5 orders of magnitude which can result in large discrepancies when used in reactive transport models to simulate geochemical reaction rates. Simulations carried out using mineral accessible surface areas (ASAs) determined from a coupled 2D and 3D imaging approach have shown better match with reaction rates measured in core-flood experiments. However, such image processing requires large amounts of time and resources. In this work, the possibility of estimating mineral ASAs from easily measured properties like mineral abundance and porosity is explored. Six sandstone samples of varying compositions were studied along with data from three additional samples from previous literature. Mineral ASAs were quantified using a combined 2D SEM and 3D X-ray nano-CT imaging approach. Sample properties like mineral accessibility, mineral ASAs, connected porosity, and clay content were compared to explore potential correlations between properties. Overall, it was observed that mineral accessibility can be predicted where feldspar mineral accessibility generally increases with increasing abundance and quartz accessibility decreases with increasing clay content. Mineral ASAs vary between samples, depending on the relative abundance of minerals and overall pore connectivity. While the ASA of quartz decreases with abundance, albite and carbonate mineral ASAs increase with abundance. Quantitative observations, including predictive relationships for ASAs from porosity and mineral volume fraction are developed. Estimations of ASAs and mineral accessibility from more easily quantifiable properties can largely reduce the required extent of image analysis.

Keywords: Image processing, mineral property quantification, accessible mineral surface area, mineral dissolution rates, reactive surface area, 3D computed tomography.

1. Introduction

Geochemical reactions occur in a variety of environmental systems, such as chemical weathering on the surface of the earth[1–5], CO_2-brine-mineral interactions in carbon capture and storage (CCS) systems[6–12], enhanced oil recovery[13–16], and subsurface energy storage systems.[17–20] These reactions are rather complex as natural environmental systems are often heterogeneous. For example, the CO_2-induced geochemical reactions in subsurface storage systems are impacted by many factors such as injection rate, formation depth, porosity, permeability, saturation, mineral composition, etc. [21]

Reactive transport modeling is a powerful tool that has been used to simulate these complex geochemical reactions over laboratory and geological timescales. [22–28] Transition state theory (TST) [29–31] is commonly used to calculate mineral reaction rates in these simulations as given by:

$$R_m = A_m k_m [f \Delta G_r] \qquad (1)$$

where R_m is the mineral reaction rate, A_m is the mineral reactive surface area, k_m is the reaction rate constant, and $f \Delta G_r$ is the thermodynamic driving force for the reaction.[32] Thermodynamic parameters and rate constants are often obtained from a thermodynamic and kinetic database, while the porosity, mineral abundance, and mineral surface areas are usually measured. X-ray diffraction (XRD) is commonly used to determine the mineral composition (abundance) of a sample, while mineral-specific surface area is often used as an approximation of reactive surface area and measured using the Brunauer–Emmett–Teller (BET) adsorption method.[33] The limitations of these approaches, however, need to be considered and may restrict the ability to accurately simulate the rate and extent of geochemical reactions and the corresponding impact of reactions on formation properties (e.g., porosity, permeability). Quantification of minor mineral phases, for example, is challenging with XRD and largely depends on the detection limit of the instrument, which can vary from 0.33% to 5%.[34] It can also be challenging to quantify clay abundance and composition through XRD analysis. Detecting clay minerals is necessary because it plays an important role in controlling pore connectivity and mineral accessibility as they are commonly present as grain coating or bridging phases.[35–39] The BET adsorption method provides a good estimation of mineral-specific surface area (SSA). However, estimating the specific surface area for each mineral in a multi-mineral sample is not feasible and instead requires analysis of pure mineral phases, which vary widely.[40,41] BET anlaysis also depends on the degassing condition and how much the sample is disaggregated[42–44]. Moreover, the mineral-specific surface area may not accurately reflect the reactive surface area of mineral phases in consolidated samples.[45]

Imaging has emerged as a relatively new approach for mineral property quantification[45–50] that has shown promise to improve simulations of mineral reaction rates. Beckingham et al. (2017) found that simulations carried out using mineral accessible surface area (ASA) quantified from imaging reflect the reaction rates observed in core-flood experiments more closely than simulations that use specific surface area.[45] In addition, imaging can often facilitate the quantification of mineral phases with abundances less than the XRD detection limit.[51]

Although the mineral abundances and accessible mineral surface areas quantified from imaging are promising for improved reactive transport modeling, the time and resources involved in this process, from sample preparation, image acquisition, image segmentation, and mineral properties quantification, can be enormous. Resources may be somewhat reduced by capturing images at lower resolutions where differences in mineral volume fractions and ASAs extracted from 0.3 microns, and 5.7 microns resolution images were found to be relatively minor (within one order of magnitude).[49] Additional limitations, however, arise from the fact that getting higher-quality images from scanning electron microscopy (SEM) requires samples to be polished and cut into thin sections.[52] As such, a means of estimating accessible mineral surface areas from other, more easily measured properties is highly desirable to reduce time and resource requirements and predict the evolution of ASA in reactive systems. In this work, we evaluate mineral ASAs of sandstones of varying compositions and explore relationships between mineral abundance, accessibility, ASA, clay content, and pore connectivity. Through analysis of these relationships, we aim to be able to estimate and predict mineral accessibility and ASAs without the intensive image acquisition and analysis process.

2. Materials and Methods

Data from nine sandstone samples were selected for analysis in this work. This includes six sandstone samples where mineral abundances and accessibilities were analyzed via SEM imaging in our previous work.[53] In addition, data from three samples from earlier literature are considered. This includes a Paluxy sandstone sample studied by Qin and Beckingham (2019)[49], collected from the pilot CO_2 injection site at Kemper County, Mississippi, U.S.[54], a Lower Tuscaloosa sandstone sample studied by Landrot et al. (2012)[47] collected from a geologic carbon sequestration pilot site in Cranfield, Mississippi (well CFU 31-F2), and a sample extracted from a geothermal well (Vydmantai-1) at a depth of 954.6 m, located at the southeast end of the Baltic Sea in Lithuania.[50] Sample characteristics and imaging methodologies are described in the following sections.

2.1 Sample characterization and preparation

The nine sandstone samples of varying compositions, including high to low clay and carbonate content, selected for this work are given in Table 1. Table 2 provides information about sample sizes used for imaging in this study and prior literatures. Core samples from the Bandera Grey, Bandera Brown, Bentheimer, and Kentucky formations obtained from Kocurek Industries and Lower Tuscaloosa and Paluxy sandstone samples obtained from the Geological Survey of Alabama were used here for 3D X-ray nano-Computed Tomography (X-ray nano-CT) imaging. Core samples from Kocurek Industries were 0.5 inches in diameter and 1 inch in length. Samples from the Geological Survey of Alabama were intact pieces roughly 0.5 x 0.5 x 0.5 in^3 in dimension. Polished thin and thick sections from each formation were created and analyzed via SEM imaging by Salek et al. (2022).[53]

Data on sample porosity, connected porosity, mineral abundances, and accessibilities were taken from the previous literature (Table 1 & Table 3) as determined using imaging analyses. All sandstones considered here are mainly composed of quartz (66% - 94%), with varying amounts of feldspar, carbonate, and clay minerals as well as trace amounts of other mineral species. The porosity of these samples varies from 13% to 35% (Table 1). [40,53,55,56]

Available ASA data were also collected from the literature for the Paluxy[49] and Lower Tuscaloosa[47] samples. Mineral ASAs for the remaining seven samples were determined here, leveraging mineral accessibility analyses from Salek et al. (2022)[53] and Ma et al. (2021).[50] For the Baltic Sea sample, the mineral segmented map obtained from Ma et al. (2021)[50] is analyzed again to determine the connected porosity and mineral accessibility considering pore connectivity.

Table 1. Sandstone samples considered in this work categorized based on relative abundances of clay and carbonate: 1) high clay, high carbonate content samples; 2) high clay, low carbonate content samples and 3) low clay, low carbonate content samples. Data from prior literature analysis in [a]Salek et al. (2022)[53], [b]Qin and Beckingham (2019)[49], [c]Ma et al. (2021)[50], [d]Landrot et al. (2012)[47].

Sample category	Formations	Quartz (v%)	Clay (v%)	Carbonate (v%)	Porosity (%)	Connected Porosity (%)
High clay and high carbonate content	Bandera Grey[a]	63.46	6.39	5.69	15.31	2.21
	Paluxy[b]	76.45	8.23	9.63	25.16	23.38

	Baltic Sea sample[c]	59.35	8.12	14.79	17.68	2.56
High clay and low carbonate content	Bandera Brown[a]	73.48	5.96	0.01	22.17	8.91
	Kentucky[a]	62.58	11.73	0	13.25	4.27
	Lower Tuscaloosa[d]	82.3	12.5	0	16	12
Low clay and low carbonate content	Lower Tuscaloosa[a]	92.03	3.67	1.48	33.29	28.69
	Bentheimer[a]	95.32	1.64	0	34.92	18.45
	Paluxy[a]	69.31	2.5	0.78	18.77	5.36

Table 2. Sample description for 2D SEM and 3D X-ray nano-CT imaging. Data from prior literature analysis in [a]Salek et al. (2022)[53], [b]Qin and Beckingham (2019)[49], [c]Ma et al. (2021)[50], [d]Landrot et al. (2012)[47].

Formations	SEM Imaging	3D X-ray nano-CT

Bandera Grey, Bandera Brown, Bentheimer, Kentucky[a]	Polished Disk of 1-in diameter and 0.2-in thickness[a]	Core Sample, 0.5-in diameter and 1 in height
Lower Tuscaloosa and Paluxy sandstone[a]	Polished thin sections[a]	Intact pieces roughly 0.5 in x 0.5 in x 0.5 in
Paluxy sandstone[b]	Polished thin section[b]	Intact piece roughly 0.5 in x 0.5 in x 0.5 in[b]
Baltic Sea[c]	Polished thin section[c]	-
Lower Tuscaloosa[d]	Polished thin section[d]	Rectangular volume (8 mm × 3 mm ×3 mm)[d]

2.2 Imaging acquisition and mineral properties quantification

3D X-ray nano-CT images of six sandstone samples were collected and used to determine pore connectivity and mineral ASA after Landrot et al. (2012)[47], Beckingham et al. (2017)[45], and Qin and Beckingham (2019)[49]. Mineral ASA reflects the surface area in contact with the reactive fluid. Mineral ASAs were computed by multiplying the average connected surface area determined from the analysis of the processed 3D X-ray nano-CT image for each sample by the mineral accessibility calculated from 2D SEM images for each phase determined in Salek et al. (2022).[53] Mineral accessibilities were computed from 2D mineral maps based on processed

SEM backscattered electron (BSE) images complemented with elemental maps from SEM energy-dispersive x-ray spectroscopy (EDS) analysis. In the processed mineral map, each mineral phase was depicted as a unique color. Accessible mineral pixels of each phase were identified as those adjacent to connected pore pixels, and mineral accessibility was calculated as the fraction of interfacial pixels corresponding to each mineral phase. Connected porosity considered here includes multi-scale nano-pore connectivity via clay minerals.[53]

Here, 3D X-ray nano-CT images were taken of the six sandstone samples studied in Salek et al. (2022)[53] using a ZEISS Xradia 620 Versa 3D X-ray Microscope at Auburn University. The reconstructed 3D X-ray nano-CT images were used to calculate the total connected surface area. This was accomplished by first manually segmenting the images into grain and pore voxels using ImageJ, an open source image processing software. Randomly sampled sub-cubes with the same total area as the corresponding 2D mineral map used to quantify mineral accessibilities were then sampled from the larger 3D image. The connected surface area of these cubes was then identified and calculated using a marching cubes algorithm in MATLAB with a mesh applied to the grain voxels. Ten of these sub-cubes were randomly selected and analyzed to obtain average values of connected surface area for each sample.

A correction factor (CF) is also needed when there is a large difference in the resolution of the 2D SEM BSE and 3D X-ray nano-CT images.[47] The CF is introduced to refine the connected surface area measured from the 3D X-ray nano-CT images in order to account for the features present at scales below the voxel size of the images. The CF was determined by first reducing the image resolution of the mineral maps in ImageJ to be matched with the resolution of the 3D X-ray nano-CT images, and then counting the number of connected interfacial pixels in the two images. The correction factor is calculated as,

$$\text{Correction factor } (CF) = \frac{P_{original}}{P_{reduced}}$$

where $P_{original}$ and $P_{reduced}$ refer to the total number of connected interfacial pixels in the original high-resolution 2D mineral map images and the resolution-reduced 2D mineral map images, respectively.[47] The corrected total connected surface area was then calculated by multiplying the connected surface area measured from 3D X-ray nano-CT images by the corresponding sample-specific correction factor.

While for the Lower Tuscaloosa[47] and Paluxy[49] samples, the accessibility and ASA data were collected from the associated papers, and the accessibility and connected porosity for the Baltic Sea sample were produced here. Then the accessibility of the minerals was multiplied by the total specific surface area determined by a method other than the 3D microCT measurement used in this study. The details of their total specific surface area calculation can be found in Ma et al. (2021).[50]

3. Results and Discussion

3.1 Image processing and mineral property quantification

3D X-ray nano-CT images were produced and processed to identify the connected pore-space and calculate the surface area for six sandstone samples.

Mineral ASAs for each of these samples were then computed using the computed surface area in conjunction with mineral accessibilities obtained from Salek et al. (2022).[53] For brevity, images and data for the Lower Tuscaloosa formation are presented here and the rest of the 3D X-ray nano-CT images are presented in the Supplementary Material. The resulting mineral ASAs for each sample are given in Table 3 in addition to mineral volume fractions and accessibilities determined from 2D mineral maps (Salek et al. (2022)[53]). It should be noted that this methodology is only valid for non-clay minerals[47] and as such the ASA of clay minerals and minerals with many small-scale features (e.g., muscovite) cannot be directly measured from these images and therefore are not reported here.

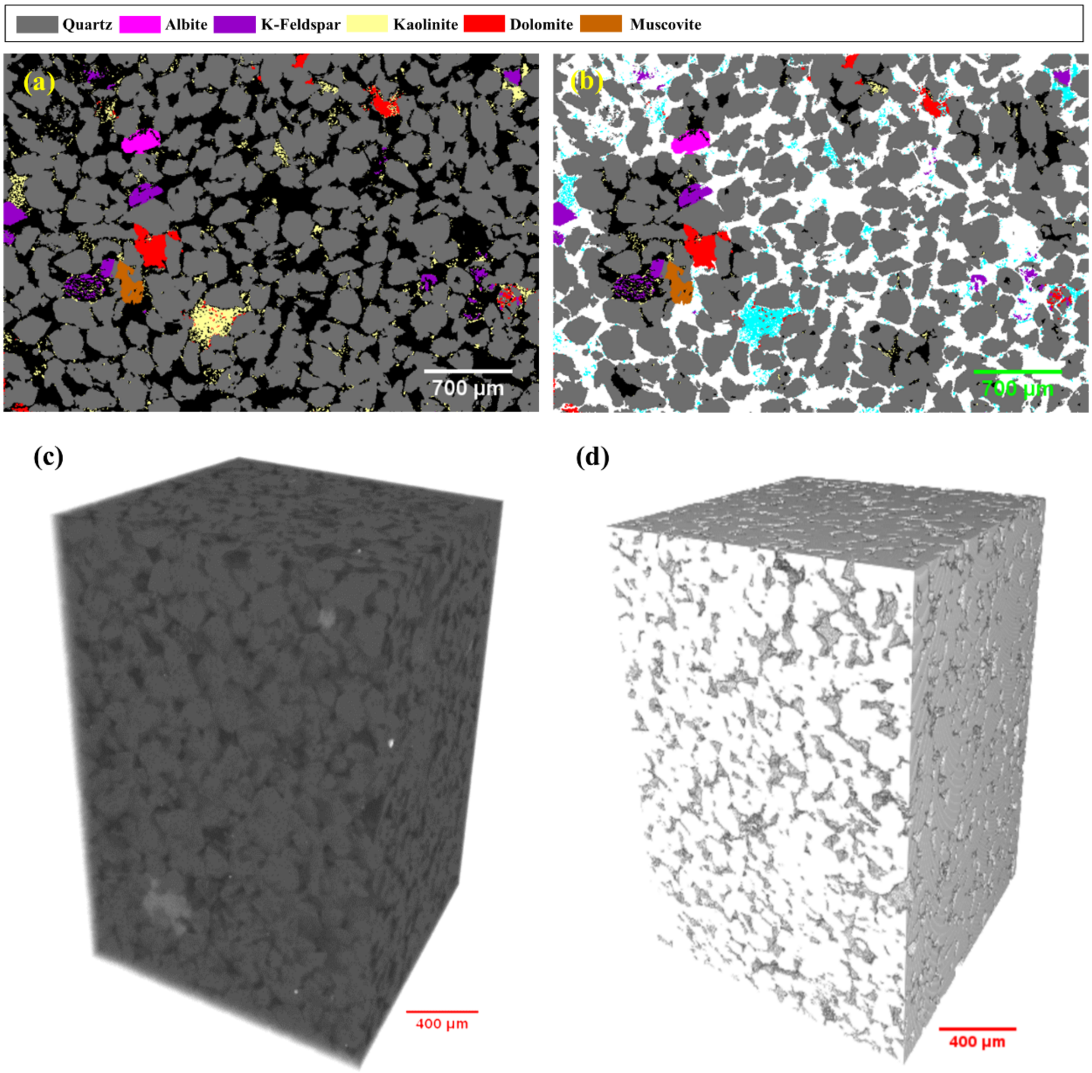

Figure 1. a) Mineral phase segmented map of Lower Tuscaloosa sample; b) connected pore space map considering nanopore connectivity showing connected macro pores as white pixels and connected nanopores in cyan; c) reconstructed 3D X-ray nano-CT image with a voxel size of 4.53 µm; d) thresholded 3D X-ray nano-CT image with pores depicted in black and grains in white; Subfigures a-b reproduced with permission from Ref. 53[53], Copyright 2022 ACS Publications.

Figure 1 shows the 2D processed mineral map for the Lower Tuscaloosa sandstone sample[53] where each color corresponds to a different mineral phase. The mineral abundances and accessibilities, determined from pixel counting, are given in Table 3. This sample is comprised of over 92% quartz with 3.67% kaolinite clay. The abundances of other mineral phases are all below 2%. The quantification of pore pixels in the processed 2D image showed that the porosity for this sample is 33%, whereas the connected porosity is 28.69% obtained from the quantification of connected pores in the 2D connected pore space map (Figure 1b). This connectivity accounts for macro-pore as well as nano-pore connectivity through clay minerals, predominantly kaolinite in this sample.

In the context of this study, macro-pores refer to the larger pore spaces which are observable with 2D SEM images and nano pores are nanometer scale pores that are beyond the SEM image resolution of this work. Nano-pore connectivity refers the connectivity in sub-resolution nano-scale pore spaces [47]. This nano-pore connectivity is special because it may make a mineral grain accessible to reactive fluid even if that phase is coated with clay, if the clay mineral has sufficient nano-pore connectivity [45,47,57]. This nano-pore connectivity can be identified and quantified via nanometer resolution Focused Ion Beam-Scanning Electron Microscopy (FIB-SEM) images of that mineral [45,47]. This information can be incorporated into the image analysis to account for nano-pore connectivity when evaluating overall pore connectivity and mineral accessibility. Excluding nano-pore connectivity can result in underestimating accessible surface area, which may provide imprecise estimates of reactivity in reactive transport simulations. For example, Salek et al. (2022) observed an increase in accessibility of K-feldspar as high as 17 times when they considered nanopore connectivity compared to when it was excluded [57].

Mineral accessibilities consider mineral surfaces in contact with the identified connected pores, where kaolinite has notably higher accessibility as compared to abundance due to its presence as a grain coating. Mineral ASAs account for connectivity in 3D as determined via analysis of the X-ray nano-CT images and are given in Table 3. There is a difference of two orders of magnitude variation between the calculated mineral ASAs for different mineral phases. The ASA of quartz is calculated to be 2.96×10^{-1} m^2/g, while the ASAs of K-feldspar, albite, and dolomite are approximately two orders of magnitude smaller. In this case, the higher ASA corresponds to the phase with the highest abundance and K-feldspar, albite, and dolomite are all minor mineral phases with abundances < 2% and accessibility <3%.

Table 3. Mineral properties, including mineral abundances, accessibilities, and ASAs quantified from 2D SEM BSE images and 3D nano-CT images. The surface area of clay minerals (kaolinite, smectite/illite, and chlorite) and muscovite cannot be directly quantified from images. Accessibility accounts for nanoscale pore connectivity through clay minerals.

Formation	Mineral	Abundance (v%)	Accessibility (%)	Accessible surface area (m^2/g)

Bandera Brown	Quartz	73.48	54.81	$4.00x10^{-02}$
	K-feldspar	8.33	5.48	$4.00x10^{-03}$
	Albite	10.24	6.02	$4.93x10^{-03}$
	Calcite	0.01	0.00	0.0
	Kaolinite	4.31	21.83	NA
	Smectite/illite	1.17	6.35	NA
	Chlorite	0.48	3.45	NA
	Anatase	0.47	0.08	$5.84x10^{-05}$
	Magnetite	1.49	1.97	$1.44x10^{-03}$
Lower Tuscaloosa	Quartz	92.03	79.48	$2.96x10^{-01}$
	K-feldspar	1.58	2.40	$8.95x10^{-03}$
	Muscovite	0.53	0.18	NA
	Kaolinite	3.67	15.51	NA
	Dolomite	1.48	2.13	$7.94x10^{-03}$
	Albite	0.49	0.30	$1.12x10^{-03}$

Bentheimer	Quartz	95.32	80.05	1.49 x10^{-02}
	K-feldspar	2.71	2.99	5.55 x10^{-04}
	Kaolinite	1.64	16.71	NA
	Calcite	0.00	0.00	0.0
	Ilmenite	0.40	0.24	4.46 x10^{-05}
Kentucky	Quartz	62.58	34.29	7.69 x10^{-02}
	Albite	16.79	10.37	2.33 x10^{-02}
	K-feldspar	2.95	4.97	1.11 x10^{-02}
	Smectite/illite	11.73	31.25	NA
	Ilmenite	0.29	0.99	2.22 x10^{-03}
	Magnetite	2.60	12.27	2.75 x10^{-02}
	Anatase	0.17	0.71	1.59 x10^{-03}
	Zircon	0.37	0.34	7.62 x10^{-04}
	Muscovite	2.55	4.79	NA
Paluxy	Quartz	69.31	47.24	6.88 x10^{-02}

	K-feldspar	1.21	1.05	1.53 x10^{-03}
	Calcite	0.78	0.96	1.40 x10^{-04}
	Kaolinite	2.26	28.12	NA
	Muscovite	0.60	0.95	NA
	Albite	24.50	17.86	2.60 x10^{-02}
	Siderite	0.29	0.35	5.10 x10^{-04}
	Anatase	0.81	0.24	3.49 x10^{-04}
	Smectite/illite	0.24	3.24	NA
Bandera Grey	Quartz	63.46	62.63	3.41 x10^{-02}
	K-feldspar	12.12	5.53	3.02 x10^{-03}
	Albite	10.22	7.45	4.06 x10^{-03}
	Calcite	5.69	0.84	4.58 x10^{-04}
	Smectite/illite	6.39	23.45	NA
	Muscovite	0.69	0.00	NA
	Biotite	1.14	0.00	0.0

	Anatase	0.29	0.09	4.91 x10^{-05}
Baltic Sea	Quartz	59.35	37.09	1.56 x10^{-02}
	K-feldspar	11.60	5.76	2.42 x10^{-03}
	Dolomite	14.79	3.03	1.27 x10^{-03}
	Kaolinite	8.13	47.85	NA
	Muscovite	5.74	5.88	NA
	Ilmenite	0.39	0.39	1.65 x10^{-04}

Comparison of data for the other sandstone samples shows that minerals with high abundance and accessibility do not necessarily have higher ASA. For example, the abundance and accessibility of K-feldspar in the Bandera Gray sandstone are 12.12% and 5.53%, whereas the abundance and accessibility of K-feldspar in the Kentucky sandstone is 2.97% and 4.97%. However, the ASA of K-feldspar in the Kentucky sample is 1.11x10^{-02} m^2/g, which is higher than the surface area of K-feldspar in the Bandera Gray sample (3.02x10^{-03} m^2/g). This indicates that abundance and accessibility alone are not a reliable means of predicting ASA. As such, correlations between measured properties are further explored.

3.2 Correlation of quantified mineral properties

In this section, relationships among mineral abundance, accessibility, ASA, and total connected surface area are explored for all nine sandstone samples. Mineral accessibilities account for multi-scale (macro and nano) pore connectivity. To evaluate the potential impact of clay and carbonate content on mineral properties, samples were separated into three categories based on clay and carbonate content (Table 1). In addition, four minerals are considered here for analysis – quartz, K-feldspar, albite, and carbonate minerals which include calcite and/or dolomite. These phases are present in a majority of the samples considered. BET-specific surface areas from the literature are also considered to compare with ASA determined from images.

3.2.1 Accessibility versus abundance

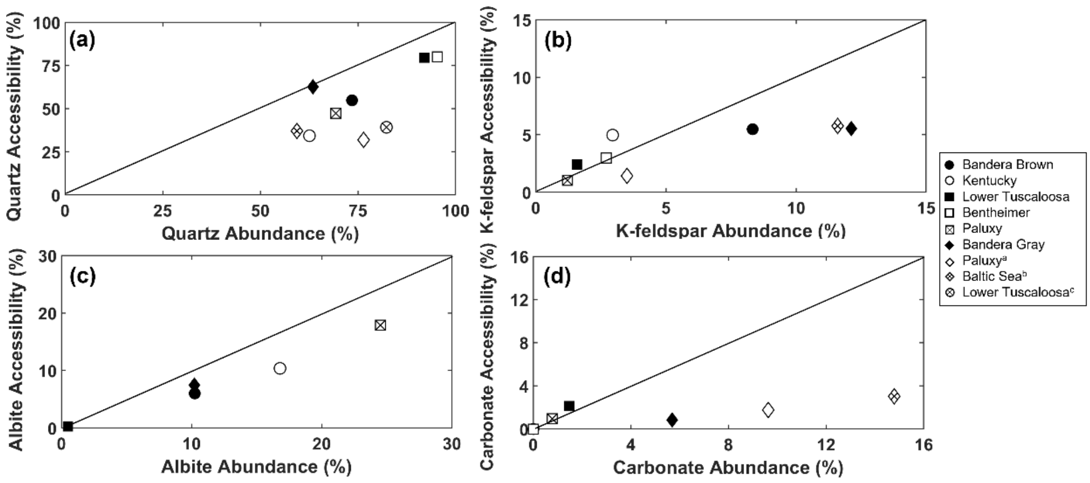

Figure 2. Relationship between mineral abundance and mineral accessibility for a) quartz, b) K-feldspar, c) albite, and d) carbonate minerals. The solid diagonal represents the equivalent line. Diamonds are data points of samples with high clay and high carbonate content, circles are samples with high clay and low carbonate

content, and squares are samples with low clay and low carbonate content. [a]Paluxy sandstone sample in Qin and Beckingham (2019)[49]; [b]Baltic Sea sample in Ma et al. (2021)[50]; [c]Lower Tuscaloosa sandstone sample in Landrot et al. (2012).[47]

Mineral accessibilities are plotted against abundances in Figure 2, with the solid line indicating equivalency between accessibility and abundance. Any data point on this solid line means that accessibility equals abundance. From Figure 2, quartz is the most abundant phase and has the highest accessibility. However, most data points fall under the equivalency line indicating quartz is relatively less accessible than suggested by mineral abundance. This reflects the grain coatings that are frequently observed on quartz surfaces. For the samples with lower clay and carbonate content (squares in Figure 2a), the quartz accessibility is relatively proportional to abundance. This makes sense as clay and carbonate minerals are often present as grain coating and bridging phases which would reduce the accessibility of the predominant phases.

The impact of clay and carbonate content on accessibility can be considered by comparing samples with low to high clay and carbonate content, shown as different symbols in Figure 2. The accessibility of quartz is quite varied for the range of sample compositions considered and is largely reduced for some samples (Paluxy, [c]Lower Tuscaloosa, and Kentucky) with higher clay and carbonate content (Figure 2a, diamond, and circular shapes), indicating clay and carbonate content has a large impact on the accessibility of quartz. This is anticipated due to the distribution of clay and carbonate phases as grain coating and bridging phases.

The accessibility of feldspar minerals, K-feldspar, and albite, increases with abundance. Compared to K-feldspar, the accessibility of albite is reflected relatively well by abundance and is less impacted by the clay or carbonate content. For the considered samples, K-feldspar is less accessible when the sample has higher clay and higher carbonate content (Figure 2b, diamond shapes) as compared to low clay and low carbonate (squares, Figure 2b). In comparison with quartz, the accessibility of feldspar minerals has better overall agreement with the observed abundances. While present in lower abundances, this may suggest that clay and carbonate minerals preferentially occur on quartz surfaces over feldspars.

As for carbonate minerals, making inferences about the overall trend is limited as only some samples contain carbonate minerals. However, the accessibility of carbonate minerals was less than the abundance for samples with high amounts of clay and carbonate (diamond shape, Figure 2d). This reflects the presence of carbonate minerals as cements between grains with associated more limited surfaces in contact with pores as evident in Figure 1, for example. For samples with lower carbonate abundances, the accessibility agrees relatively well with abundance.

3.2.2 Accessible surface area vs. abundance

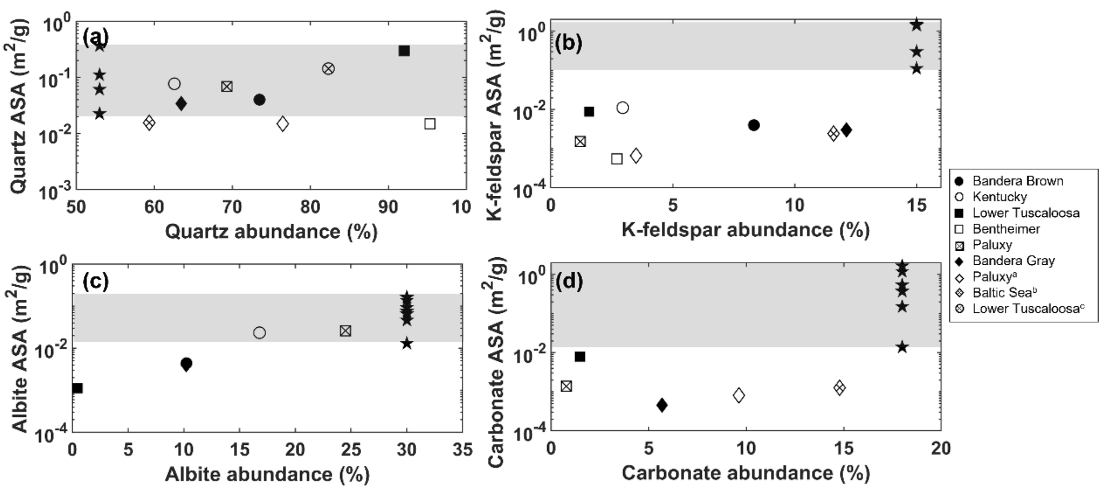

Figure 3. Relationship between mineral abundance and mineral ASA: a) quartz, b) K-feldspar, c) albite, and d) carbonate minerals. Diamonds are data points of samples with high clay and high carbonate content, circles are samples with high clay and low carbonate content, and squares are samples with low clay and low carbonate content. BET-specific surface areas reported in the literature are plotted with the star shape, and their range shaded grey (abundances for these values are meaningless). BET literature data: Quartz (Brady and Walther (1989)[58]; Gautier et al. (2001)[59]; Tester et al. (1994)[60]), K-feldspar (Gautier et al. (1994)[61]; Lundstrom and Ohman (1990)[62]; Blake and Walter (1996)[63]; Bunsenberg and Clemency (1975)[64]), Albite (Knauss and Wolery (1986)[65]; Chou and Wollast (1984)[66]; Wang et al. (2017)[67]; Hellmann (1994)[68]; Chen and Brantley (1997)[69]), Carbonate (Cubillas et al. (2005)[70]; Papadopoulos and Rowell (1988)[71]; Sjoberg (1976)[72]; Subhas et al. (2015)[73])

Mineral ASAs are plotted against mineral abundance in Figure 3. Aside from the two Lower Tuscaloosa samples, the ASA of quartz decreases within an order of magnitude with increasing quartz abundance. This may reflect that samples with higher quartz content have less surface roughness as the presence of clay minerals results in increased roughness. Quartz ASAs agree relatively well with the range of measured BET surface areas (stars and shaded range) for quartz. The observed higher quartz ASA for the two Lower Tuscaloosa samples reflects that these are samples whose pores are more well-connected compared to the other samples considered here.

ASAs for K-feldspar (Figure 3b) are relatively consistent and one to more than three orders of magnitude less than the BET surface area values obtained from the literature. The lower ASA for K-feldspar minerals here reflects the low accessibility of K-feldspar minerals in the considered samples (Table 3). The accessibility of K-feldspar for all samples is <6%, even for samples with larger proportions of K-feldspar (>10% abundance). As such, the resulting ASA is reduced as these phases are not adjacent to the connected pore space. The BET surface areas do not reflect mineral accessibility and are thus higher for K-feldspar samples. While K-feldspar ASA is independent of K-feldspar abundance, the ASA of albite increases with increasing abundance and interestingly better agrees with the range of BET surface area measurements. This may be because of the better agreement between Albite accessibility and abundance, discussed above.

The highest observed ASA of carbonate minerals occurs in samples low carbonate content (<5%). For samples comprised of >5% carbonate minerals, the surface area is relatively constant with carbonate abundance. There is a wide range of BET-measured surface area values from the literature for carbonate minerals, all larger than the ASA values measured in this study. This discrepancy reflects the observed relation between carbonate abundance and accessibility where for samples with >5% carbonate minerals, the accessibility of carbonate minerals is low.

3.2.3 Variation in accessibility with clay content

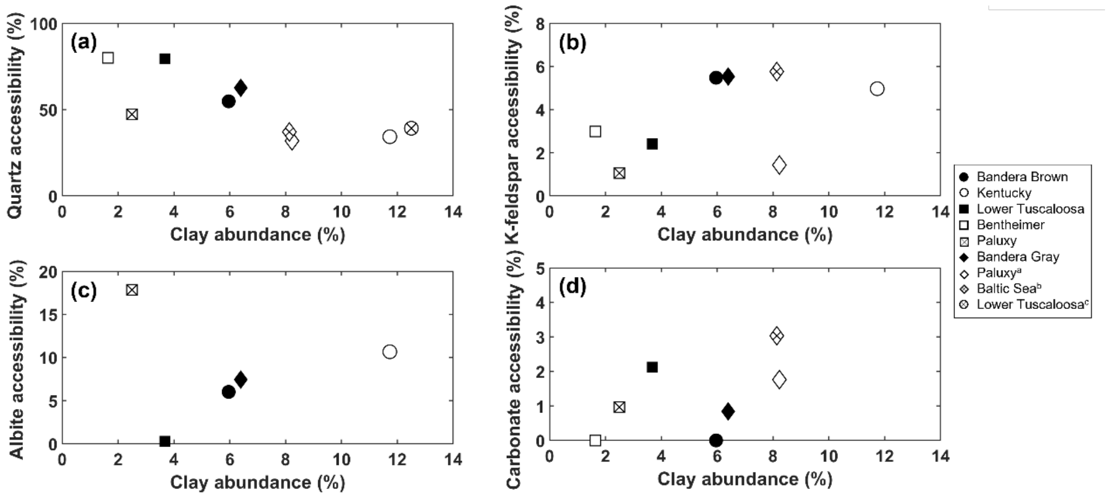

Figure 4. Relationship between mineral accessibility and clay abundance for a) quartz, b) K-feldspar, c) albite, and d) carbonate minerals. Samples with high clay and high carbonate content are represented by diamond markers, samples with high clay and low carbonate content are marked with circles, and samples with low clay and low carbonate content are marked with squares. [a]Paluxy sandstone sample in Qin and Beckingham (2019)[49]; [b]Baltic Sea sample in Ma et al. (2021)[50]; [c]Lower Tuscaloosa sandstone sample in Landrot et al. (2012).[47]

Clay minerals are typically present as coating or bridging phases and can potentially impact the overall pore connectivity and accessibility of mineral surfaces. [46,74] Mineral accessibility is plotted against clay abundance in Figure 4 to evaluate the potential impact of clay abundance on mineral accessibilities. As shown in the figure, the accessibility of quartz is most impacted by clay abundance, decreasing as the clay abundance increases. When the clay content is greater than 8%, the accessibility of quartz is less than 50%. The accessibility of K-feldspar and albite overall increase with increasing clay content, except for the Paluxy sample from Kemper County, Mississippi (hollow diamond in Figure 4b). Carbonate accessibility increases with clay abundance for samples with low clay low carbonate content (squares in Figure 4d) but overall carbonate accessibility is low such that a predictive relationship is challenging to discern.

3.2.4 Dependence of mineral ASA on porosity and connected porosity

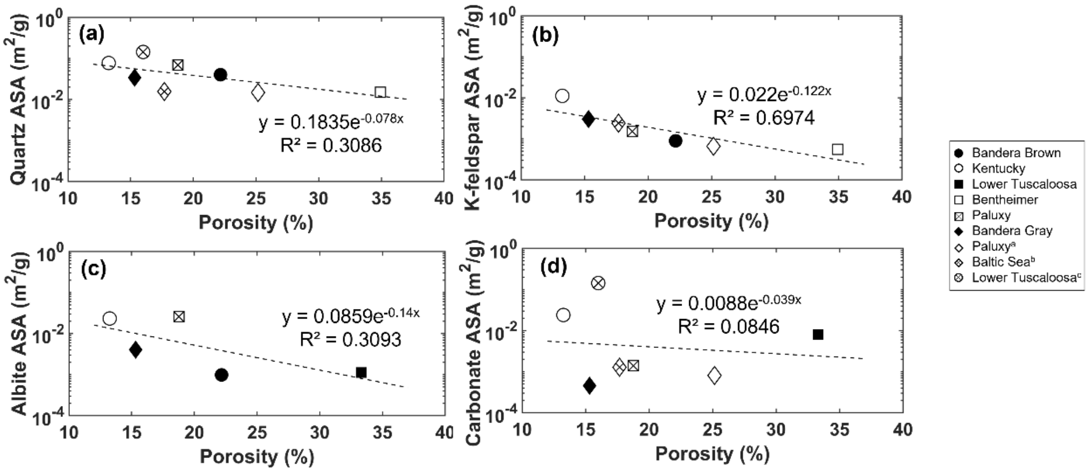

Figure 5. Relationship between mineral ASA and porosity for a) quartz, b) K-feldspar, c) albite, and d) carbonate minerals. Exponential regression curve shown in dotted lines. Samples with high clay and high carbonate content are represented by diamond markers, samples with high clay and low carbonate content are marked with circles, and samples with low clay and low carbonate content are marked with squares. [a]Paluxy sandstone sample in Qin and Beckingham (2019)[49]; [b]Baltic Sea

sample in Ma et al. (2021)[50]; [c]Lower Tuscaloosa sandstone sample in Landrot et al. (2012)[47].

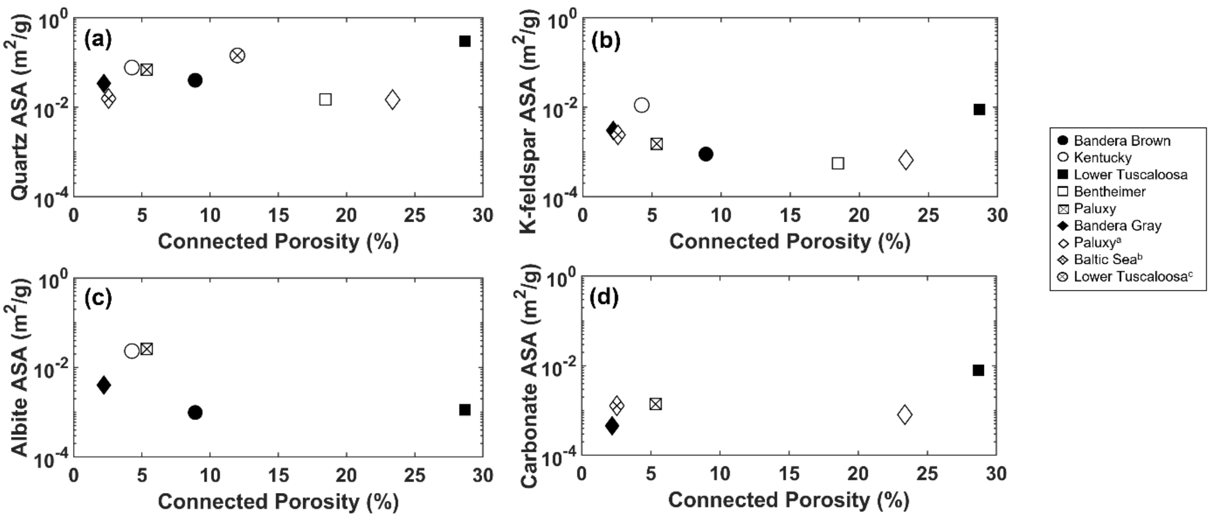

Figure 6. Relationship between mineral ASA and connected porosity for a) quartz, b) K-feldspar, c) albite, and d) carbonate. Samples with high clay and high carbonate content are represented by diamond markers, samples with high clay and low carbonate content are marked with circles, and samples with low clay and low carbonate content are marked with squares. [a]Paluxy sandstone sample in Qin and Beckingham (2019)[49]; [b]Baltic Sea sample in Ma et al. (2021)[50]; [c]Lower Tuscaloosa sandstone sample in Landrot et al. (2012)[47].

The relationship between sample porosity and connected porosity and mineral ASA is explored in Figures 5 and 6. The mineral ASAs of all phases decrease with increasing porosity, with exceptions for the Lower Tuscaloosa sample (filled square). Regression trendlines are fit to data in Figure 5 to explore whether an empirical relation can be made to relate ASA to porosity. ASA values for the Lower Tuscaloosa sample are excluded for Quartz and K-feldspar from the regression analysis.

Analyses show there is a strong relationship between ASA and porosity for K-feldspar where the empirical equation fits the data well with an R^2 value of 0.69. For quartz and albite, the predictivity of the equation is moderate with R^2 values near 0.3. Carbonate mineral ASA, on the other hand, has low predictability based on porosity from this empirical relationship where the R^2 value is only 0.08. Even with moderate predictability, however, these relationships can improve estimates of ASA where common empirical approaches to estimating mineral reactive surface area result in several orders of magnitude variation in values and observed ASA values here are within one order of magnitude from the trendline for the majority of samples.

For connected porosity, quartz, K-feldspar, and albite show a similar decreasing trend, whereas carbonate ASA remains relatively consistent even with increasing connected porosity except for the Lower Tuscaloosa sample (filled square) (Figure 6). More porous sandstone samples may perhaps be more weathered and thus have lower overall roughness than lower porosity samples. Similarly, more weathered samples may have higher connected porosity.

3.2.5 Dependence of connected surface area on composition

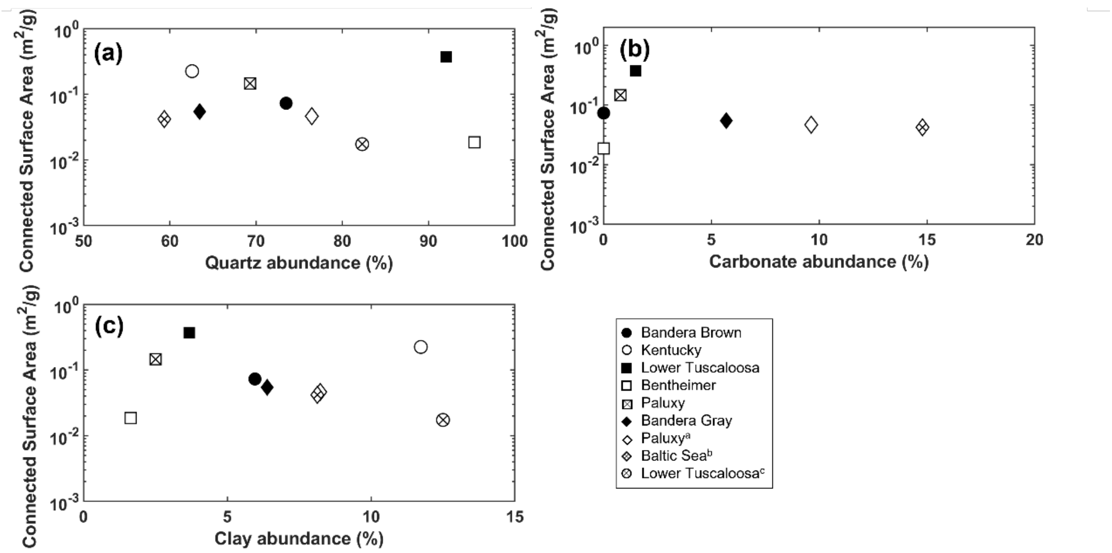

Figure 7. Relationship between the total connected surface area determined from 3D micro-CT images and mineral abundance of a) quartz, b) clays, and c) carbonates. Samples with high clay and high carbonate content are represented by diamond markers, samples with high clay and low carbonate content are marked with circles, and samples with low clay and low carbonate content are marked with squares. [a]Paluxy sandstone sample in Qin and Beckingham (2019)[49]; [b]Baltic Sea sample in Ma et al. (2021)[50]; [c]Lower Tuscaloosa sandstone sample in Landrot et al. (2012)[47].

Variations in the total connected surface area for sandstone samples is plotted against quartz, carbonate, and clay abundance in Figure 7. In general, the connected surface area decreases as quartz abundance increases (except in Lower Tuscaloosa samples), likely because of the relatively smooth surface (decreased roughness) of quartz grains. Carbonate minerals are commonly present as a cementing phase, which could potentially decrease the overall pore connectivity. For samples with carbonate content >2%, the connected surface area is relatively constant as carbonate mineral abundance increases. Increased surface area is expected with increasing clay content as clay coatings increase the overall surface roughness. Some of this roughness, however, may be beyond the image resolution and may not add to the total surface area quantified here.

Interestingly, for the high clay and high carbonate samples (diamonds), the total connected surface area remains constant with increasing quartz, carbonate, or clay abundance. The total connected surface area for the low clay, low carbonate samples (squares), on the other hand, increases with the increase of carbonate and clay content. These observations suggest that increasing carbonate content reduces the total pore connectivity and thus connected surface area while increasing clay content increases surface roughness and thus connected surface area. For the low clay, low carbonate samples, the relative proportion of clay content between samples is larger than the difference in carbonate content which may reflect the increase in ASA. Additionally, these samples only have a small fraction of carbonate mineral phases (<5%) such that overall connectivity is not largely impacted.

3.2.6 Dependence of connected surface area on mineral accessibility

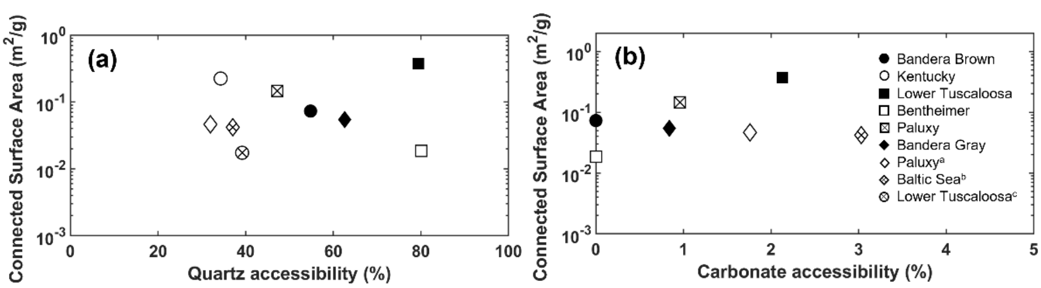

Figure 8. Relationship between the total connected surface area calculated from 3D micro-CT images and mineral accessibility for a) quartz and b) carbonate minerals.

Samples with high clay and high carbonate content are represented by diamond markers, samples with high clay and low carbonate content are marked with circles, and samples with low clay and low carbonate content are marked with squares. [a] Paluxy sandstone sample in Qin and Beckingham (2019)[49]; [b]Baltic Sea sample in Ma et al. (2021)[50]; [c]Lower Tuscaloosa sandstone sample in Landrot et al. (2012)[47].

The total connected surface area is plotted against mineral accessibility in Figure 8. Since quartz is the most abundant phase in all samples, it is studied in this part. Compared to other mineral species, the surface of quartz is relatively smooth, and samples with higher quartz accessibility are expected to have a lower surface area (Figure 8a). For carbonate minerals, samples with lower carbonate and clay content (Figure 8b, square) tend to have higher surface areas. This is likely because carbonate minerals are usually present as cementing phases, which may decrease the overall pore connectivity and thus the connected surface area. Again, for the high clay and high carbonate samples (diamonds), the total connected surface area remains constant with increasing quartz or carbonate accessibility. However, the total connected surface area for the low carbonate low clay samples (squares) increases with the increase of carbonate accessibility.

5. Conclusions

This study explores potential relationships between mineral accessibility, ASA, and the overall mineral composition using data from nine sandstone samples of varying compositions. ASAs were determined from a multi-scale imaging-based approach and data of the four most common mineral phases found in sandstone were compared here: quartz, feldspar, clay, and carbonate minerals.

Observations in this study suggest that the accessibility of quartz, K-feldspar, and albite can be estimated based on knowledge of the overall mineral composition. The accessibility of quartz can be approximated based on its abundance and the clay content of the samples. When samples have no or low clay content, the accessibility of quartz is expected to be proportional to its abundance, whereas with increasing clay content, the accessibility decreases as clay minerals often occur as coatings on quartz mineral surfaces (Figure 2). More specifically, when clay content is greater than 8%, the accessibility of quartz is less than 50%. This could be utilized to estimate mineral accessibility if the sample composition is known (e.g., XRD analysis).

The accessibility of K-feldspar and albite increase with abundance. For samples with larger proportions of albite, the accessibility can reasonably be approximated as equal to the abundance. The accessibility of feldspar minerals did not have a direct dependence on the abundance of clay minerals in contrast with quartz. This suggests clay minerals may preferentially occur on quartz surfaces in comparison to K-feldspar and albite.

In terms of carbonate minerals, predictive patterns were less clear. For samples with low volume fractions of carbonate minerals, <5%, the abundance and accessibility increased proportionally. For samples with >5% calcite abundance, the accessibility of carbonate minerals was far less. This reflects the occurrence of carbonate as grain cementing phases with limited surfaces in contact with reactive fluids.

ASAs here are quantified by multiplying mineral accessibility by the measured total connected surface area. As there was decent predictability for mineral accessibility based on mineral abundances and clay content, this suggests that ASAs may be obtained via reduced imaging efforts requiring only quantification of the total connected surface area which can be obtained via 3D X-ray nano-CT imaging. Required mineral abundances and clay content can more rapidly and easily be determined from routine XRD analyses.

Mineral ASAs largely depend on the total connected surface area, measured here from 3D X-ray nano-CT images. The total connected surface area generally decreases with increasing quartz and carbonate content because of the comparatively smooth surface of quartz and the reduction in pore connectivity due to increased cementation from carbonate minerals. Increasing clay content is anticipated to increase surface roughness but quantification of this roughness may be limited by the resolution of the 3D X-ray nano-CT images.

Some additional correlations were also observed that can more easily facilitate estimation of ASA for some mineral phases. No direct correlation could be drawn between the ASA and the abundance of the quartz. However, albite ASA increases with abundance. ASA values for minor mineral phases ($<5\%$ abundance) are difficult to predict. However, K-feldspar and carbonate ASAs appear largely independent of their abundance and relatively constant at ~$3x10^{-3}$ m^2/g and ~10^{-3} m^2/g, respectively, for samples with volume fractions >5%.

Mineral ASAs also showed some dependence on porosity and correlative equations between ASAs and porosity were fit based on collected data. As porosity is easily determined via routine core sample analysis, use of these equations would greatly improve estimation of mineral surface areas. While the fit of these relationships with the collected data was not perfect, and some outlier samples were removed to improve fit, these relationships may still improve estimates of surface area in comparison with current approaches that yield variations in surface area estimates ranging several orders of magnitude.

Acknowledgment

This work is supported by the National Science Foundation under Grant No. EAR-1847243. The purchase of the X-ray Computed Nano-tomography instrument used to obtain results included in this publication was supported by the National Science Foundation under the award CMMI MRI 1919818.

Supporting Information

Raw and Processed 3D Nano CT Images of the samples.

Abbreviations and Terminologies

SEM - Scanning Electron Microscopy

3D X-Ray nano-CT - Three-dimension X-Ray nano Computed Tomography

BET - Brunauer–Emmett–Teller

XRD - X-ray Diffraction

SSA (m^2/g) - Specific Surface Area

ASA (m^2/g) - Accessible Surface Area, the mineral surface area accessible to pore fluids

CF - Correction factor, applied to account for the sub resolution features in 3D X-ray nano-CT images

Mineral Accessibility (%) - Fraction of pore-grain interfacial pixels of each mineral phase

Porosity (%) – The ratio of void space to the total volume

Connected Porosity (%) – The ratio of connected pore space to the total volume

Total Connected Surface Area (m^2/g)- Total mineral surface area adjacent to connected pores

References

(1) Cao, Y.; Song, H.; Algeo, T. J.; Chu, D.; Du, Y.; Tian, L.; Wang, Y.; Tong, J. Intensified Chemical Weathering during the Permian-Triassic Transition Recorded in Terrestrial and Marine Successions. *Palaeogeogr. Palaeoclimatol. Palaeoecol.* **2019**, *519*, 166–177.

(2) Chen, X.-Y.; Teng, F.-Z.; Huang, K.-J.; Algeo, T. J. Intensified Chemical

Weathering during Early Triassic Revealed by Magnesium Isotopes. *Geochim. Cosmochim. Acta* **2020**, *287*, 263–276.

(3) Mahdikhani, M.; Bamshad, O.; Shirvani, M. F. Mechanical Properties and Durability of Concrete Specimens Containing Nano Silica in Sulfuric Acid Rain Condition. *Constr. Build. Mater.* **2018**, *167*, 929–935.

(4) Yu, Z.; Wu, G.; Keys, L.; Li, F.; Yan, N.; Qu, D.; Liu, X. Seasonal Variation of Chemical Weathering and Its Controlling Factors in Two Alpine Catchments, Nam Co Basin, Central Tibetan Plateau. *J. Hydrol.* **2019**, *576*, 381–395.

(5) White, A. F.; Brantley, S. L. Chemical Weathering Rates of Silicate Minerals: An Overview. *Chem. Weather. rates Silic. Miner.* **2018**, 1–22.

(6) Navarre-Sitchler, A.; Steefel, C. I.; Sak, P. B.; Brantley, S. L. A Reactive-Transport Model for Weathering Rind Formation on Basalt. *Geochim. Cosmochim. Acta* **2011**, *75* (23), 7644–7667.

(7) March, R.; Doster, F.; Geiger, S. Assessment of CO2 Storage Potential in Naturally Fractured Reservoirs with Dual-porosity Models. *Water Resour. Res.* **2018**, *54* (3), 1650–1668.

(8) Cui, H.; Zhao, T.; Wu, R. An Investment Feasibility Analysis of Ccs Retrofit Based on a Two-Stage Compound Real Options Model. *Energies* **2018**, *11* (7), 1711.

(9) Snæbjörnsdóttir, S. Ó.; Oelkers, E. H.; Mesfin, K.; Aradóttir, E. S.; Dideriksen,

K.; Gunnarsson, I.; Gunnlaugsson, E.; Matter, J. M.; Stute, M.; Gislason, S. R. The Chemistry and Saturation States of Subsurface Fluids during the in Situ Mineralisation of CO2 and H2S at the CarbFix Site in SW-Iceland. *Int. J. Greenh. Gas Control* **2017**, *58*, 87–102.

(10) Snæbjörnsdóttir, S. Ó.; Gislason, S. R.; Galeczka, I. M.; Oelkers, E. H. Reaction Path Modelling of In-Situ Mineralisation of CO2 at the CarbFix Site at Hellisheidi, SW-Iceland. *Geochim. Cosmochim. Acta* **2018**, *220*, 348–366.

(11) Bensinger, J.; Beckingham, L. E. CO2 Storage in the Paluxy Formation at the Kemper County CO2 Storage Complex: Pore Network Properties and Simulated Reactive Permeability Evolution. *Int. J. Greenh. Gas Control* **2020**, *93*, 102887.

(12) Qin, F.; Beckingham, L. E. The Impact of Mineral Reactive Surface Area Variation on Simulated Mineral Reactions and Reaction Rates. *Appl. Geochemistry* **2021**, *124*, 104852.

(13) Khurshid, I.; Afgan, I. Geochemical Investigation of CO2 Injection in Oil and Gas Reservoirs of Middle East to Estimate the Formation Damage and Related Oil Recovery. *Energies* **2021**, *14* (22), 7676.

(14) Jia, H.; Sheng, J. J. Simulation Study of Huff-n-Puff Air Injection for Enhanced Oil Recovery in Shale Oil Reservoirs. *Petroleum* **2018**, *4* (1), 7–14.

(15) Esene, C.; Rezaei, N.; Aborig, A.; Zendehboudi, S. Comprehensive Review of

Carbonated Water Injection for Enhanced Oil Recovery. *Fuel* **2019**, *237*, 1086–1107.

(16) Gbadamosi, A. O.; Junin, R.; Manan, M. A.; Agi, A.; Yusuff, A. S. An Overview of Chemical Enhanced Oil Recovery: Recent Advances and Prospects. *Int. Nano Lett.* **2019**, *9* (3), 171–202.

(17) Kabuth, A.; Dahmke, A.; Beyer, C.; Bilke, L.; Dethlefsen, F.; Dietrich, P.; Duttmann, R.; Ebert, M.; Feeser, V.; Görke, U.-J. Energy Storage in the Geological Subsurface: Dimensioning, Risk Analysis and Spatial Planning: The ANGUS+ Project. *Environ. Earth Sci.* **2017**, *76* (1), 1–17.

(18) Fleming, M. R.; Adams, B. M.; Randolph, J. B.; Ogland-Hand, J. D.; Kuehn, T. H.; Buscheck, T. A.; Bielicki, J. M.; Saar, M. O. High Efficiency and Large-Scale Subsurface Energy Storage with CO2. In *43rd Workshop on geothermal reservoir engineering, Stanford, CA*; 2018.

(19) Iloejesi, C. O.; Beckingham, L. E. Assessment of Geochemical Limitations to Utilizing CO2 as a Cushion Gas in Compressed Energy Storage Systems. *Environ. Eng. Sci.* **2021**, *38* (3), 115–126.

(20) Koohi-Fayegh, S.; Rosen, M. A. A Review of Energy Storage Types, Applications and Recent Developments. *J. Energy Storage* **2020**, *27*, 101047.

(21) Yang, F.; Bai, B.; Tang, D.; Shari, D.-N.; David, W. Characteristics of CO2 Sequestration in Saline Aquifers. *Pet. Sci.* **2010**, *7* (1), 83–92.

(22) Steefel, C. I.; Molins, S.; Trebotich, D. Pore Scale Processes Associated with Subsurface CO2 Injection and Sequestration. *Geochemistry Geol. CO2 Sequestration* **2013**, *77*, 259–303.

(23) Steefel, C. I.; DePaolo, D. J.; Lichtner, P. C. Reactive Transport Modeling: An Essential Tool and a New Research Approach for the Earth Sciences. *Earth Planet. Sci. Lett.* **2005**, *240* (3–4), 539–558.

(24) Steefel, C. *Reactive Transport Modeling: Applications in Subsurface Energy and Environmental Problems*; John Wiley & Sons, 2018.

(25) Pallud, C.; Meile, C.; Laverman, A. M.; Abell, J.; Van Cappellen, P. The Use of Flow-through Sediment Reactors in Biogeochemical Kinetics: Methodology and Examples of Applications. *Mar. Chem.* **2007**, *106* (1–2), 256–271.

(26) Li, L.; Maher, K.; Navarre-Sitchler, A.; Druhan, J.; Meile, C.; Lawrence, C.; Moore, J.; Perdrial, J.; Sullivan, P.; Thompson, A. Expanding the Role of Reactive Transport Models in Critical Zone Processes. *Earth-science Rev.* **2017**, *165*, 280–301.

(27) Boano, F.; Harvey, J. W.; Marion, A.; Packman, A. I.; Revelli, R.; Ridolfi, L.; Wörman, A. Hyporheic Flow and Transport Processes: Mechanisms, Models, and Biogeochemical Implications. *Rev. Geophys.* **2014**, *52* (4), 603–679.

(28) Maher, K.; Navarre-Sitchler, A. Reactive Transport Processes That Drive

Chemical Weathering: From Making Space for Water to Dismantling Continents. *Rev. Mineral. Geochemistry* **2019**, *85* (1), 349–380.

(29) Aagaard, P.; Helgeson, H. C. Thermodynamic and Kinetic Constraints on Reaction Rates among Minerals and Aqueous Solutions; I, Theoretical Considerations. *Am. J. Sci.* **1982**, *282* (3), 237–285.

(30) Lasaga, A. C.; Kirkpatrick, R. J. Kinetics of Geochemical Processes. 3 Vol. 8. Reviews in Mineralogy. **1981**.

(31) Lasaga, A. C. Chemical Kinetics of Water-rock Interactions. *J. Geophys. Res. solid earth* **1984**, *89* (B6), 4009–4025.

(32) Steefel, C. I.; Beckingham, L. E.; Landrot, G. Micro-Continuum Approaches for Modeling Pore-Scale Geochemical Processes. *Rev. Mineral. Geochemistry* **2015**, *80* (1), 217–246.

(33) Brunauer, S.; Emmett, P. H.; Teller, E. Adsorption of Gases in Multimolecular Layers. *J. Am. Chem. Soc.* **1938**, *60* (2), 309–319.

(34) O'Connell, K.; Regalbuto, J. R. High Sensitivity Silicon Slit Detectors for 1 Nm Powder XRD Size Detection Limit. *Catal. Letters* **2015**, *145* (3), 777–783.

(35) Storvoll, V.; Bjørlykke, K.; Karlsen, D.; Saigal, G. Porosity Preservation in Reservoir Sandstones Due to Grain-Coating Illite: A Study of the Jurassic Garn Formation from the Kristin and Lavrans Fields, Offshore Mid-Norway. *Mar. Pet. Geol.* **2002**, *19* (6), 767–781.

(36) Griffiths, J.; Worden, R. H.; Wooldridge, L. J.; Utley, J. E. P.; Duller, R. A. Detrital Clay Coats, Clay Minerals, and Pyrite: A Modern Shallow-Core Analogue for Ancient and Deeply Buried Estuarine Sandstones. *J. Sediment. Res.* **2018**, *88* (10), 1205–1237.

(37) Tang, L.; Gluyas, J.; Jones, S. Porosity Preservation Due to Grain Coating Illite/Smectite: Evidence from Buchan Formation (Upper Devonian) of the Ardmore Field, UK North Sea. *Proc. Geol. Assoc.* **2018**, *129* (2), 202–214.

(38) Wooldridge, L. J.; Worden, R. H.; Griffiths, J.; Utley, J. E. P. How to Quantify Clay-Coat Grain Coverage in Modern and Ancient Sediments. *J. Sediment. Res.* **2019**, *89* (2), 135–146.

(39) Busch, B. Pilot Study on Provenance and Depositional Controls on Clay Mineral Coatings in Active Fluvio-Eolian Systems, Western USA. *Sediment. Geol.* **2020**, *406*, 105721.

(40) Black, J. R.; Carroll, S. A.; Haese, R. R. Rates of Mineral Dissolution under CO2 Storage Conditions. *Chem. Geol.* **2015**. https://doi.org/10.1016/j.chemgeo.2014.09.020.

(41) Bourg, I. C.; Beckingham, L. E.; DePaolo, D. J. The Nanoscale Basis of CO2 Trapping for Geologic Storage. *Environ. Sci. Technol.* **2015**, *49* (17), 10265–10284.

(42) Lapham, D. P.; Lapham, J. L. Gas Adsorption on Commercial Magnesium

Stearate: Effects of Degassing Conditions on Nitrogen BET Surface Area and Isotherm Characteristics. *Int. J. Pharm.* **2017**, *530* (1), 364–376. https://doi.org/https://doi.org/10.1016/j.ijpharm.2017.08.003.

(43) SONG, J.; WANG, L.; SONG, G. Research on Influence Factors on Determination of Specific Surface Area of Carbon Materical by N2 Adsorption Method. *J. Appl. Sci. Eng. Innov. Vol* **2014**, *1* (1), 77–82.

(44) Tinni, A.; Sondergeld, C.; Rai, C. Particle Size Effect on Porosity and Specific Surface Area Measurements of Shales. In *International Symposium of the Society of Core Analysts, SCA2014-013, Avignon-France*; 2014.

(45) Beckingham, L. E.; Steefel, C. I.; Swift, A. M.; Voltolini, M.; Yang, L.; Anovitz, L. M.; Sheets, J. M.; Cole, D. R.; Kneafsey, T. J.; Mitnick, E. H.; Zhang, S.; Landrot, G.; Ajo-Franklin, J. B.; DePaolo, D. J.; Mito, S.; Xue, Z. Evaluation of Accessible Mineral Surface Areas for Improved Prediction of Mineral Reaction Rates in Porous Media. *Geochim. Cosmochim. Acta* **2017**. https://doi.org/10.1016/j.gca.2017.02.006.

(46) Peters, C. A. Accessibilities of Reactive Minerals in Consolidated Sedimentary Rock: An Imaging Study of Three Sandstones. *Chem. Geol.* **2009**, *265* (1–2), 198–208.

(47) Landrot, G.; Ajo-Franklin, J. B.; Yang, L.; Cabrini, S.; Steefel, C. I. Measurement of Accessible Reactive Surface Area in a Sandstone, with Application to CO 2 Mineralization. *Chem. Geol.* **2012**, *318–319*, 113–125.

https://doi.org/10.1016/j.chemgeo.2012.05.010.

(48) Beckingham, L. E.; Mitnick, E. H.; Steefel, C. I.; Zhang, S.; Voltolini, M.; Swift, A. M.; Yang, L.; Cole, D. R.; Sheets, J. M.; Ajo-Franklin, J. B. Evaluation of Mineral Reactive Surface Area Estimates for Prediction of Reactivity of a Multi-Mineral Sediment. *Geochim. Cosmochim. Acta* **2016**, *188*, 310–329.

(49) Qin, F.; Beckingham, L. E. Impact of Image Resolution on Quantification of Mineral Abundances and Accessible Surface Areas. *Chem. Geol.* **2019**, *523*, 31–41.

(50) Ma, J.; Ahkami, M.; Saar, M. O.; Kong, X.-Z. Quantification of Mineral Accessible Surface Area and Flow-Dependent Fluid-Mineral Reactivity at the Pore Scale. *Chem. Geol.* **2021**, *563*, 120042.

(51) Leask, E. K.; Ehlmann, B. L. Identifying and Quantifying Mineral Abundance through VSWIR Microimaging Spectroscopy: A Comparison to XRD and SEM. In *2016 8th Workshop on Hyperspectral Image and Signal Processing: Evolution in Remote Sensing (WHISPERS)*; IEEE, 2016; pp 1–5.

(52) Xiong, Q.; Baychev, T. G.; Jivkov, A. P. Review of Pore Network Modelling of Porous Media: Experimental Characterisations, Network Constructions and Applications to Reactive Transport. *J. Contam. Hydrol.* **2016**, *192*, 101–117.

(53) Salek, M. F.; Qin, F.; Asadi, P.; Iloejesi, C.; Brunhoeber, O.; Mahmood, M.;

Beckingham, L. E. Impact of Pore Connectivity on Quantification of Mineral Accessibility in Sandstone Samples. *ACS Earth Sp. Chem.* **2022**. https://doi.org/https://doi.org/10.1021/acsearthspacechem.2c00099.

(54) Riestenberg, D. *Project ECO2S: Characterization of a World Class Carbon Dioxide Storage Complex*; Southern States Energy Board, Peachtree Corners, GA (United States), 2018.

(55) Bashir, M. J. K.; Isa, M. H.; Kutty, S. R. M.; Awang, Z. Bin; Aziz, H. A.; Mohajeri, S.; Farooqi, I. H. Landfill Leachate Treatment by Electrochemical Oxidation. *Waste Manag.* **2009**, *29* (9), 2534–2541. https://doi.org/10.1016/j.wasman.2009.05.004.

(56) Areir, M.; Xu, Y.; Harrison, D.; Fyson, J. 3D Printing of Highly Flexible Supercapacitor Designed for Wearable Energy Storage. *Mater. Sci. Eng. B Solid-State Mater. Adv. Technol.* **2017**, *226* (June), 29–38. https://doi.org/10.1016/j.mseb.2017.09.004.

(57) Salek, M. F.; Qin, F.; Asadi, P.; Iloejesi, C.; Brunhoeber, O.; Mahmood, M.; Beckingham, L. E. Impact of Pore Connectivity on Quantification of Mineral Accessibility in Sandstone Samples. *ACS Earth Sp. Chem.* **2022**, *6* (7), 1858–1867.

(58) Brady, P. V; Walther, J. V. Controls on Silicate Dissolution Rates in Neutral and Basic PH Solutions at 25 C. *Geochim. Cosmochim. Acta* **1989**, *53* (11), 2823–2830.

(59) Gautier, J.-M.; Oelkers, E. H.; Schott, J. Are Quartz Dissolution Rates Proportional to BET Surface Areas? *Geochim. Cosmochim. Acta* **2001**, *65* (7), 1059–1070.

(60) Tester, J. W.; Worley, W. G.; Robinson, B. A.; Grigsby, C. O.; Feerer, J. L. Correlating Quartz Dissolution Kinetics in Pure Water from 25 to 625 C. *Geochim. Cosmochim. Acta* **1994**, *58* (11), 2407–2420.

(61) Gautier, J.-M.; Oelkers, E. H.; Schott, J. Experimental Study of K-Feldspar Dissolution Rates as a Function of Chemical Affinity at 150 C and PH 9. *Geochim. Cosmochim. Acta* **1994**, *58* (21), 4549–4560.

(62) Lundström, U.; Öhman, L. Dissolution of Feldspars in the Presence of Natural, Organic Solutes. *J. Soil Sci.* **1990**, *41* (3), 359–369.

(63) Blake, R. E.; Walter, L. M. Effects of Organic Acids on the Dissolution of Orthoclase at 80 C and PH 6. *Chem. Geol.* **1996**, *132* (1–4), 91–102.

(64) Busenberg, E.; Clemency, C. V. The Dissolution Kinetics of Feldspars at 25 C and 1 Atm CO2 Partial Pressure. *Geochim. Cosmochim. Acta* **1976**, *40* (1), 41–49.

(65) Knauss, K. G.; Wolery, T. J. Dependence of Albite Dissolution Kinetics on PH and Time at 25 C and 70 C. *Geochim. Cosmochim. Acta* **1986**, *50* (11), 2481–2497.

(66) Chou, L.; Wollast, R. Study of the Weathering of Albite at Room Temperature

and Pressure with a Fluidized Bed Reactor. *Geochim. Cosmochim. Acta* **1984**, *48* (11), 2205–2217.

(67) Wang, J.; Wang, Z.; Yang, L.; Yang, G.; Miao, C.; Lv, P. Natural Albite as a Novel Solid Basic Catalyst for the Effective Synthesis of Biodiesel: Characteristics and Performance. *Energy* **2017**, *141*, 1650–1660.

(68) Hellmann, R. The Albite-Water System: Part I. The Kinetics of Dissolution as a Function of PH at 100, 200 and 300 C. *Geochim. Cosmochim. Acta* **1994**, *58* (2), 595–611.

(69) Chen, Y.; Brantley, S. L. Temperature-and PH-Dependence of Albite Dissolution Rate at Acid PH. *Chem. Geol.* **1997**, *135* (3–4), 275–290.

(70) Cubillas, P.; Köhler, S.; Prieto, M.; Chaïrat, C.; Oelkers, E. H. Experimental Determination of the Dissolution Rates of Calcite, Aragonite, and Bivalves. *Chem. Geol.* **2005**, *216* (1–2), 59–77.

(71) Papadopoulos, P.; Rowell, D. L. The Reactions of Cadmium with Calcium Carbonate Surfaces. *J. Soil Sci.* **1988**, *39* (1), 23–36.

(72) Sjöberg, E. L. A Fundamental Equation for Calcite Dissolution Kinetics. *Geochim. Cosmochim. Acta* **1976**, *40* (4), 441–447.

(73) Subhas, A. V; Rollins, N. E.; Berelson, W. M.; Dong, S.; Erez, J.; Adkins, J. F. A Novel Determination of Calcite Dissolution Kinetics in Seawater. *Geochim. Cosmochim. Acta* **2015**, *170*, 51–68.

(74) Lai, P.; Moulton, K.; Krevor, S. Pore-Scale Heterogeneity in the Mineral Distribution and Reactive Surface Area of Porous Rocks. *Chem. Geol.* **2015**, *411*, 260–273.